Biophysical Journal
Article

Biophysical Society

Structure of the gel phase of diC22:1PC lipid bilayers determined by x-ray diffraction

John F. Nagle,[1,*] Nathaniel Jennings,[1] Weiheng Qin,[1] Daniel Yan,[1] Stephanie Tristram-Nagle,[1] and Frank Heinrich[1,2]

[1]Department of Physics, Carnegie Mellon University, Pittsburgh, Pennsylvania and [2]Center for Neutron Research, National Institute of Standards and Technology, Gaithersburg, Maryland

ABSTRACT High-resolution x-ray data are reported for the ordered phases of long-chain di-monounsaturated C22:1 phosphocholine lipid bilayers. Similar to PC lipids that have saturated chains, diC22:1PC has a subgel phase and a gel phase, but dissimilarly, we find no ripple phase. Our quantitative focus is on the structure of the gel phase. We have recorded 17 lamellar orders, indicating a very well-ordered structure. Fitting to a model provides the phases of the orders. The Fourier construction of the electron density profile has two well-defined headgroup peaks and a very sharp and deep methyl trough. The wide-angle scattering exhibits two Bragg rods that provide the area per molecule. They have an intensity pattern quite different than that of lipids with saturated chains. Models of chain packing indicate that ground state chain configurations are tilted primarily toward next nearest neighbors with an angle that is also consistent with the modeling of the electron density profile. Wide-angle modeling also indicates broken mirror symmetry between the monolayers. Our wide-angle results and our electron density profile together leads to the hypothesis that the sn-1 and sn-2 chains have equivalent penetration depths in contrast to the gel phase structure of lipids with saturated hydrocarbon chains.

SIGNIFICANCE Biophysical understanding of membranes is greatly enhanced by simulations that provide a level of molecular detail unobtainable experimentally. However, simulations depend upon the force fields chosen. Training force fields on well-determined experimental data is de rigueur. Although much experimental data exists for the fully fluid phase bilayers of greatest biological relevance, relatively more and better structural data exist for the lower temperature ordered phases of bilayers composed of lipids with saturated chains. This paper provides equal-quality structural data for a lipid with unsaturated double bonds that can be used to evaluate force fields for this biologically important variation of the hydrocarbon chains.

INTRODUCTION

Bilayers of lipids with saturated hydrocarbon chains, such as the very well-studied DPPC and DMPC lipids, have several liquid crystalline thermodynamic phases. In a sequence of increasing order as the temperature is lowered, they are the fluid phase, the ripple phase, the gel phase, and the subgel phase. The comparison of their structures has been illuminating (1–3). Importantly, the experimental results have been used to train and validate the force fields used in simulations. Although most comparisons have been made for the biologically more relevant fluid phase (4–12), more extensive structural data is available for some low temperature phases, and this provides even more stringent tests of force fields (13–18).

In contrast to saturated lipids, the study of lipid bilayers with unsaturated chains has only focused on the fluid phase. The most-studied lipid with a double bond in each of its 18-carbon chains is DOPC (19–21). However, its fluid phase extends down to –17°C, below which it is difficult to work with fully hydrated samples. Taking advantage of the main transition temperature increasing with longer chain lengths, we have turned to studying ordered phases of bilayers of diC22:1PC. This phosphocholine lipid has two 22-carbon chains with a double bond between the 13th and 14th carbon on each chain and a convenient chain melting temperature of 13°C. Although diC22:1PC is an uncommon lipid biologically, the ordered phases of bilayers composed of different chain lengths of di-monounsaturated PC lipids

Submitted September 13, 2022, and accepted for publication December 21, 2022.

*Correspondence: nagle@cmu.edu

Editor: Tommy Nylander.

https://doi.org/10.1016/j.bpj.2022.12.030

likely have homologous structures, and it constitutes a valid testing ground for force fields.

The first notable difference compared with saturated PCs is that the diC22:1PC bilayer does not have a ripple phase. We found a very well-characterized gel phase as well as a subgel phase with interesting thermodynamic behavior, as shown in Section I of supporting material. However, the structure of subgel phases is famously difficult to obtain unambiguously, even for DPPC (22–24), so we have not attempted that for diC22:1PC. This work focuses on obtaining a gel phase structure for diC22:1PC of comparable quality to those obtained for saturated lipids (25,26). Our main structural data are from two varieties of x-ray diffraction. Wide-angle scattering (WAXS) obtains information about the in-plane structure, and low-angle scattering (LAXS, often called SAXS in the membrane literature, although the angles are not very small) obtains the electron density profiles along the direction perpendicular to the bilayer. Together they obtain a quite detailed structure of the gel phase of diC22:1PC.

MATERIALS AND METHODS

Sample preparation

Lipid diC22:1PC (1,2-C22:1-*sn*-glycero-phosphocholine) was purchased from Avanti Polar Lipids (Alabaster, AL) in the lyophilized form and used as received. Oriented samples consisting of stacks of approximately 1600 bilayers were prepared using the "rock and roll" method (27,28). 4 mg of lipid in high-performance liquid chromatography-grade organic solvent (Aldrich, Milwaukee, WI) trifluoroethanol:chloroform (2:1, v/v) was deposited onto a flat Si wafer (15 mm by 30 mm) that had been heated to 40°C and maintained in a warm atmosphere inside a glove-box. After rapid evaporation and while rocking the substrate, an immobile film formed, which was then further dried for several hours in a vacuum chamber to evaporate residual organic solvent. Samples were trimmed to occupy 5 mm by 30 mm within the middle of the Si substrate. The thickness of the sample (used for the x-ray absorption correction (25)) was estimated from the lipid mass, covered substrate area, and the amount of water required to obtain the measured lamellar repeat *D*-spacing.

X-ray data acquisition protocol

The flat oriented sample was mounted in our x-ray sample chamber, which provides greater than 99% tunable relative humidity (29). Two x-ray sources were used. An in-house rotating anode (Rigaku RUH3R) provided CuK_α x-rays with wavelength 1.5418 Å focused by a Fox2D collimator (Xenocs, Sassenge, France). Data were recorded on a Mercury CCD (Rigaku, Woodlands, TX). Our highest-quality wide-angle data were obtained on beamline ID7A1 at the Cornell High Energy Synchrotron Source (CHESS) with wavelength 0.8434 Å selected by a W/B_4C multilayer monochromator with a wavelength spread of 1% and recorded on an Eiger 4M (2 K × 2 K) detector (Dectris AG, Baden-Daettwil, Switzerland).

The flat oriented sample was rotated about an axis perpendicular to the beam, parallel to the Si wafer, and located within the sample (29). A negative lower limit of the rotation blocked the sample from the x-ray beam. The upper limit was chosen to obtain specular scattering from all orders whose Bragg angles were small enough to pass through the exit window of the sample chamber. The beam height perpendicular to the substrate for zero rotation angle was chosen to guarantee that the 5 mm part of the sample in the direction of the beam remained in the beam for all rotation angles, thereby assuring that the appropriate Lorentz factor was essentially proportional to q. The beam width in the plane of the stack of bilayers was 1.0 mm for the in-house setup. As the wide-angle scattering is less intense, data were also taken at the CHESS synchrotron but with a narrower and better focused beam (0.2 mm) to reduce geometric broadening. Previous studies of DPPC from this lab (30) have reported average in-plane DPPC gel domains as large as 2900 Å and roughly 600 Å perpendicular to the substrate in the fluid phase (31), equivalent to a domain volume of about 1 μm^3. As the sample volume in the beam is 10^7 μm^3, one expects the effectively continuous mosaic distribution that was observed (32).

WAXS data and chain modeling

For the gel phase, there are two Bragg rods, BR1 and BR2, that have varying intensities as a function of q_z along fixed in-plane values. The intensity for each value of q_z was obtained by integrating the intensity above background along the q_r direction. Scattering from subgel phases has weaker Bragg rods at smaller values of q_r that would be consistent with headgroup ordering. The absence of such scattering in the gel phase implies that there is no headgroup ordering. Also, there is no indication of in-plane correlations between adjacent bilayers. Therefore, we analyzed the WAXS scattering with models of hydrocarbon chain packing in a single bilayer. Consistent with the appearance of only two instead of three Bragg rods and following the convention used for the DPPC gel phase, a nonprimitive unit cell was assumed to be orthorhombic (distorted hexagonal) (22) with perpendicular dimensions a in the x direction and b in the y direction.

Packing considerations strongly suggest that the hydrocarbon chain unit cell contains two identical chains in each monolayer, consistent with the (1,0) and (0,1) Bragg rods being extinct. Fig. 1 *a* shows two in-plane unit cells where one chain intersects in the middle of the rectangular unit cell and the other intersects at a corner. We chose $a > b$, so the nonextinct Bragg rods with the smallest q_r are indexed as $(\pm 2, 0)$ and $(\pm 1, \pm 1)$. Because the sample is an in-plane powder with many domains with a uniform distribution of angles relative to the beam, there is simultaneous scattering from all six Bragg rods. For an orthorhombic unit cell, the four $(\pm 1, \pm 1)$ rods scatter with the same q_{r11} value, and the experimentally observable intensity is their sum that we simply call (1, 1). The two $(\pm 2, 0)$ rods scatter with the same q_{r20} value, and we call that sum (2, 0). The unit cell dimensions are obtained from $q_{r20} = 4\pi/a$ and $q_{r11} = 2\pi/(a^{-2}+b^{-2})^{1/2}$. There are two choices for the unit cell corresponding to how (1, 1) and (2, 0) are assigned to BR1 and BR2. The first choice, which we call UC1, identifies (1, 1) with BR1, and the other choice, which we call UC2, identifies (1, 1) with BR2. Fig. 1 *a* shows these two choices of the in-plane real-space unit cell that have two reciprocal space Bragg rods at the same two q_r locations.

For the contents of the unit cell, we assumed that each chain was in its conformational ground state that consists of *trans* methylenes for carbons C2–C12 and C15–C21, a *cis* double bond for C13–C14, and ending with the terminal methyl for C22 as shown in Fig. 1 *b* and c. Packing dictates that the chains in each monolayer be parallel with the same offset of the *cis* double bonds in the z-direction. Fig. 1 *c* shows the double bonds in the upper monolayer located near 10.5 Å. Chains in the opposite monolayer have z-positions of opposite signs, and the distance, Δz, between opposing methyls near the bilayer center was set so that the ratio of the methyl to the methylene volume is ≈ 2, conforming with the LAXS models. The caption to Fig. 1 identifies this as the Δz offset. Chains in the opposite monolayers may have different in-plane offsets with respect to the unit cell; the relative differences in these offsets are named Δx and Δy. Although it would be possible for the monolayers to be uncoupled, in which case Δx and Δy would be uniformly distributed in an ensemble, let us here provide the description of coupled monolayers, which turns out to be the viable class of models. The chain carbons lie in a plane, which means that there is an angle φ between the x axis of the unit cell and where that plane intersects the unit cell. In Fig. 1, φ is nearly 90°, so the zig-zag chain plane is more apparent in Fig. 1 *c* than in Fig. 1 *b*. The carbon plane can also be tilted in two ways. The angle θ rotates it about a horizontal axis in the carbon plane, which is apparent by the tilted chains in Fig. 1 *b*. Subsequently, the angle ψ rotates the chains about an axis perpendicular to the carbon plane, which

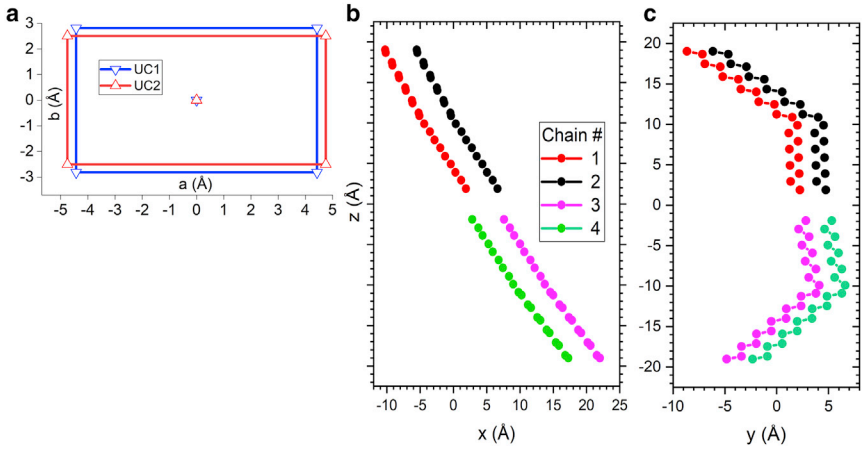

FIGURE 1 (*a*) Two in-plane *x*-*y* unit cells that have the same Bragg rod q_r locations. (*b*) Projections of the carbon backbones of four chains in the *x*-*z* plane and (*c*) in the *y*-*z* plane. Parameter values discussed in the text are $\varphi = 83$, $\theta = 38$, $\psi = -18$, $\Delta x = 0.71$ *a*, $\Delta y = 0.92$ *b*, and $\Delta z = 1.9$ Å. To see this figure in color, go online.

shows up mainly in Fig. 1 *c*. These three Euler angles may be different for the upper (U) and lower (L) monolayers. The main distinction is that $\varphi_L = \varphi_U$ gives mirror symmetry when $\Delta x = \Delta y = 0$ and $\theta = \psi = 0$, in contrast to $\varphi_L = \varphi_U + \pi$ for which there is inversion symmetry. For both symmetries, one can also choose equal or opposite values of θ and of ψ. The initial symmetry in Fig. 1 is a mirror symmetry, as can be best seen in Fig. 1 *c* and by undoing the θ rotation in Fig. 1 *b*.

Given choices of the above structural parameters, chain carbon positions were input into a Python program that calculated the sum of the atoms' scattering amplitudes, assigning nine, eight, and seven electrons, respectively, to methyl, methylene, and methine carbons. Atomic form factors and explicit locations of hydrogens were not used as they make little difference within the experimental WAXS range. The amplitude squared was then calculated for all relevant ($\pm$m, $\pm$n) Bragg rods, which were then appropriately summed to compare to the BR1 and BR2 experimental scattering intensities. The program was verified to reproduce the well-known WAXS pattern for DMPC (27,33). To find the best WAXS model, a grid search over the above model parameters was performed to determine which structure best agreed with the Bragg rod intensities as a function of q_z.

D. Repeat spacings and peak intensities

The lamellar spacing from each exposure was determined by the value of *D* that best fits the peak positions in pixels, p_h, for all orders *h*:

$$p_h = p_0 + \left(S/pix\right)\tan\left(2\sin^{-1}\left(h\lambda/2D\right)\right), \qquad (1)$$

where *S* is the distance from sample to detector (123 mm for in-house data and 422 mm for CHESS data), and *pix* is the pixel size (68 μm for in-house data and 75 μm for CHESS data). The reciprocal space locations q_h of the h^{th} order were then $2\pi h/D$. One advantage of our experimental setup for oriented samples is that the *D*-spacing can be varied by varying the relative humidity, providing a range of *q*-values for the Fourier form factor $F(q)$ (25).

Background scattering was measured by setting the substrate at a negative angle to block scattering from the sample and calculated to mimic background scattering. Additional residual background was subtracted from each peak separately. The integrated peak intensity was then summed within a rectangular pixel area; the width of the rectangle was increased with increasing order to ensure inclusion of the same number of mosaic domains for each order. Intensities overlapped between adjacent peaks, thereby exaggerating the peak intensity of weak orders adjacent to and riding on the tails of strong orders. As shown in Fig. S4, this was corrected by positioning the box boundaries in the q_z-direction to equate the intensities of the overlapping tails calculated from the peak heights and Lorentzian widths after having determined that the peaks were adequately represented by Lorentzians (32). Relative uncertainties from the background subtraction for the stronger peak were typically less than 1%. However, different exposures were consistent with larger uncertainties. Standard errors σ_h for strong orders were obtained from exposures of nearly the same *D*-spacing. In contrast, the $h = 10$ order was unobservable. Zero intensity is, of course, a real and important result, but the assigned uncertainty should clearly not be zero or infinity; it was instead taken to be equal to the uncertainties assigned to the well-quantified $h = 9$ and $h = 11$ orders. Similar uncertainties were assigned to other weak orders. Finally, an absorption correction was made to correct for less absorption of the beam in the sample itself as the order increased (25).

Determination of the electron density profile ρ(z)

The electron density profile $\rho(z)$ along the bilayer normal *z* for symmetric bilayers is given by

$$\rho(z) = \rho_w + \left(1/D\right)\left[F(0) + 2\sum_h F(q_h)\cos(zq_h)\right]. \qquad (2)$$

ρ_w is the electron density of water. $F(q_h)$ is the form factor for $q_h = 2\pi h/D$, where *h* is the index of the order, and *D* is the lamellar repeat spacing of the sample. The absolute value of the $h > 0$ form factor for oriented samples is

$$|F(q_h)| = \left(q_h \cdot I_h\right)^{1/2}/K_e, \qquad (3)$$

where I_h is the intensity of order *h*, q_h is the Lorentz factor in the small angle approximation, and K_e is the usual scale factor that takes account of experimental conditions such as total x-ray exposure and amount of sample. The value of the form factor at $q = 0$ is given by (34)

$$F(0) = 2(n_L - \rho_w V_L)/A \qquad (4)$$

where $n_L = 498$ is the number of electrons in diC22:1PC, $\rho_w = 0.3345$ e/Å^3 is the electron density of water at T = 10°C, V_L is the molecular volume, and *A* is the area per lipid.

Although symmetry constrains each $F(q_h)$ to be either +1 or −1, there remains a formidable 2^{17} phase problem for employing Eq. (2) that was solved using electron density models. We first employed the SDP software (21) that requires Gaussian functional forms for many of the components. We obtained a better fit using a more flexible composition-space model that describes all molecular components by pairs of error functions, in

which the spatial extension along the bilayer normal, z, and the interfacial roughness, σ, on either side can be separately parameterized (35). Further, the Monte Carlo Markov Chain (MCMC)-based global optimizer *Dream,* implemented in the analysis package *bumps,* provided an efficient search of the entire parameter space and yielded robust confidence intervals on fit parameters (36).

The inputs to the fitting software are the intensities I_h (absorption and Lorentz corrected) and their uncertainties. The program calculates the initial model form factors $F_M(q_{eh}, P)$, where P denotes the values of the initial model parameters. The MCMC global optimizer identifies the model parameter values P and experimental scale factors K_e that minimize

$$\chi^2 = \sum_e \sum_h \sigma_{eh}^{-2} \left(|K_e F_e(q_{eh})|^2 - |F_M(q_{eh}, P)|^2 \right)^2 \quad (5)$$

where σ_{eh} is the experimental uncertainty for each order h and exposure e. The model thereby estimates the phase factors (± 1 for symmetric bilayers) for all values of q and the scale factors K_e for each experimental data set.

RESULTS

Phase behavior

An oriented sample was incubated in a refrigerator near 5°C for over a year. The x-ray pattern shown in Fig. S1 had the earmarks of a subgel phase. Interestingly, it did not melt into a typical fluid phase until the temperature was increased above 15°C. This subgel phase did not reappear upon cooling. This intriguing phase behavior involving subgel phases is similar to that of DPPC. Details are elaborated in section I of the supporting material.

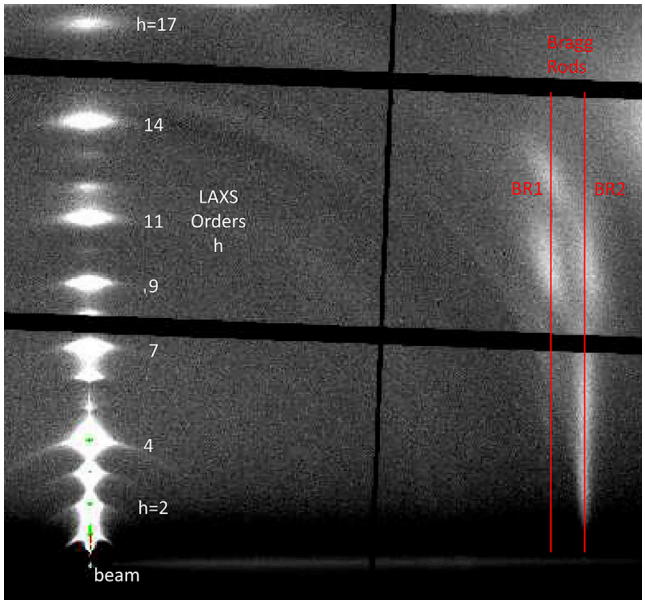

FIGURE 2 Gel phase scattering measured at CHESS at $T = 10$°C. Grey-scale intensity from zero (black) to a maximum cutoff (white). The highest visible lamellar order along the meridian ($q_r = 0$, varying q_z) is $h = 17$. The D-spacing was 69.3 Å. The WAXS Bragg rod loci are indicated with thin vertical red lines. Bragg rod 1 has little intensity at small q_z and occurs at $q_r = 1.32$ Å^{-1}. Bragg rod 2 occurs at $q_r = 1.42$ Å^{-1}. On-line colored pixels indicate the highest peak intensities for orders $h = 1$–4. To see this figure in color, go online.

When the temperature was lowered from the fluid phase to below T = 13°C, we always obtained the x-ray scattering pattern shown in Fig. 2. The WAXS scattering exhibits two Bragg rods, typical of gel phases, but no intermediate Bragg rods like those in Fig. S1, which are characteristic of subgel phases. The intensities of the lamellar LAXS orders are different for gel and subgel phases (see also Fig. S2). Still, both have much stronger higher orders than the fluid phase; that is well understood as due to the smaller bending modulus of the F phase dispersing the intensity of the lamellar orders into diffuse scattering (37).

In-plane gel phase structure

The WAXS data consist of two Bragg rods that intersect the equator (q_z=0) at q_{BR1}=1.32 Å^{-1} and q_{BR2}=1.42 Å^{-1}. These can be indexed in a 2D in-plane body-centered orthorhombic unit cell with Miller indices (2,0) and (1,1) in two ways. The unit cell dimensions a and b in the respective x and y directions follow directly. Their values are shown in Table 1 for the two unit cells, UC1 and UC2. The product of a and b gives the area A for an integral number of chains. These areas are consistent with the lateral packing of two hydrocarbon chains in each monolayer, so A is the area per lipid.

Fig. 3 shows the intensities $I(q_z)$ of the two Bragg rods BR1 and BR2 identified in Fig. 2. The intensities integrated over q_z are roughly equal for BR1 and BR2, although intensities for small q_z are likely undercounted due to the substrate cutting off scattering as it is rotated. We have performed a grid search over the chain model parameters to find the chain packing model that best predicts the experimental intensities in Fig. 3. The most significant experimental feature to discriminate between models is the presence of

TABLE 1 WAXS results for the alternate orthorhombic unit cells, UC1 and UC2, from the (2,0) and (1,1) Bragg rods are shown in the upper rows. The lower rows show results of model fitting from WAXS intensity data. Uncertainties are shown in column 3. Column 4 shows values for DPPC obtained from WAXS data at $T = 20$°C (30). Units are appropriate powers of Å.

1	2	3	4
WAXS	UC1	UC2	DPPC
q_{20}	1.42	1.32 (0.01)	1.48
q_{11}	1.32	1.42 (0.01)	1.33
a	8.86	9.50 (0.1)	8.5
b	5.63	5.01 (0.05)	5.6
A	49.9	47.6 (0.9)	47.9
Θ	N/A	42.5 (2)	31.6
D_C	N/A	20.5 (1.0)	17.3
V_{HC}	N/A	976 (67)	829
V_H	N/A	331 fixed	331
V_L	N/A	1307 (67)	1148
D_B	N/A	54.9 (1.8)	48.4
D	N/A	69.2 LAXS	63.4
n_W	N/A	11.8 (1.6)	12.6

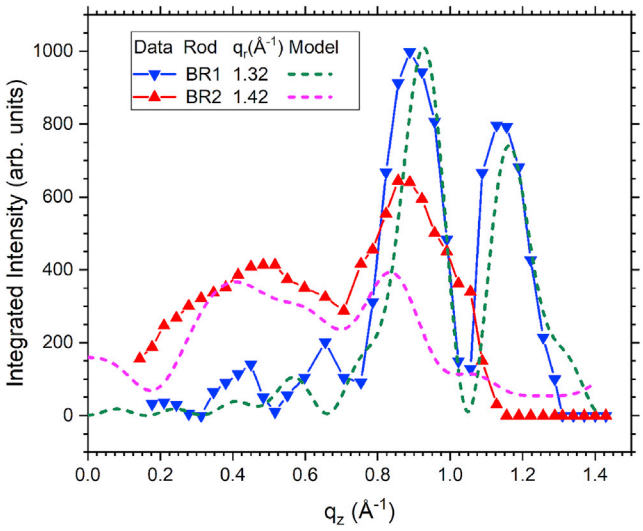

FIGURE 3 Solid symbols show experimental intensities along q_z for the two Bragg rods, BR1 (*downward-pointing triangles*) and BR2 (*upward-pointing triangles*). Corresponding curves with no symbols show the best fits for the bilayer model using UC2. To see this figure in color, go online.

the two peaks in BR1 at large q_z. Importantly, no bilayer model with the UC1 unit cell reproduced this feature. This feature was also not reproduced when assuming two uncorrelated monolayers, in which case the total scattering would be like that from a single monolayer.

After an extensive five-parameter grid search, we have zoomed in on a UC2 model that has Bragg rod intensities that compare favorably with the experimental data in Fig. 3. The real-space bilayer model is shown in Fig. 1. The two monolayers basically have mirror symmetry that is then broken by the tilt angles and by the lateral offsets, especially Δx in the a-direction. It is noteworthy that both the data and the calculated model indicate two smaller peaks at smaller q_z in the BR1 Bragg rod. Such features appear in Bragg rods of gel phases of saturated chain lipids, where they have been called satellites, as they are analogous to the secondary and tertiary maxima of single-slit diffraction patterns. The unusual feature here compared with saturated lipids (25) is that the BR1 peak is split into two peaks, which the model reproduces. Despite considerable searching, the model intensity for BR2 does not compare as favorably to the experiment as for BR1. Nevertheless, the calculated intensity for BR2 is relatively featureless compared with BR1, as is the experimental intensity in Fig. 3.

This modeling of the hydrocarbon chain packing gives an overall tilt Θ of the chains that is significantly larger than the chain tilt in DPPC. This then gives a hydrocarbon thickness D_C and a hydrocarbon volume $V_{HC} = AD_C$ with values shown in column 3 in Table 1. Table 1 continues by assuming that the headgroup volume V_H is the same as for DPPC to obtain an estimated total lipid volume V_L. The average (Luzzati) bilayer thickness D_B is then $2V_L/A$. The number of water molecules per lipid is $n_W = A(D - D_B)/2V_W$ where D is the measured average repeat spacing and $V_W = 29.9$ Å^3 at $T = 10°C$ is the volume of a bulk water molecule.

Transverse gel phase structure

Fig. 4 shows the experimental form factors $|F(q_h)|$ from seven exposures at different lamellar D-spacings. Importantly, unlike fluid phases, some higher-order form factors remain strong, even stronger than for the DPPC gel phase. This implies that the C22:1PC gel structure is highly ordered. Fig. 4 also shows the continuous form factor obtained by simultaneously fitting an electron density model to the measured intensities. By varying the hydration level, data sets were taken when the sample had different lamellar repeat D-spacings and therefore different $q_h = 2\pi h/D$. Therefore, one sees significant slopes in $F(q)$ in several q-regions; these slopes are reproduced quite well by the model.

The model not only gives the absolute $|F(q)|$ in Fig. 4, but it also gives the signs of F(q) and thereby provides a likely solution to the phase problem. The model $F(q)$ changes sign each time $|F(q)|$ bounces off zero. Notably, there is no sign change near $q = 0.7$ Å^{-1}. Starting from the positive value of $F(0)$ required by Eq. 4, Fig. 4 shows the signs for each experimental $|F(q_h)|$. Then, the $+/-$ phase factors from Fig. 4 allow the Fourier construction of the electron density profile using Eq. (2) for each data set. Fig. 5 shows the average of the seven Fourier electron density profiles. There is a deep methyl trough at $z = 0$. That is followed by a nearly constant hydrocarbon plateau. Of course, the Fourier transform has superimposed wiggles due to finite truncation of orders, but it does suggest a somewhat larger electron density for the C2–C12 methylenes than for the C15–C21

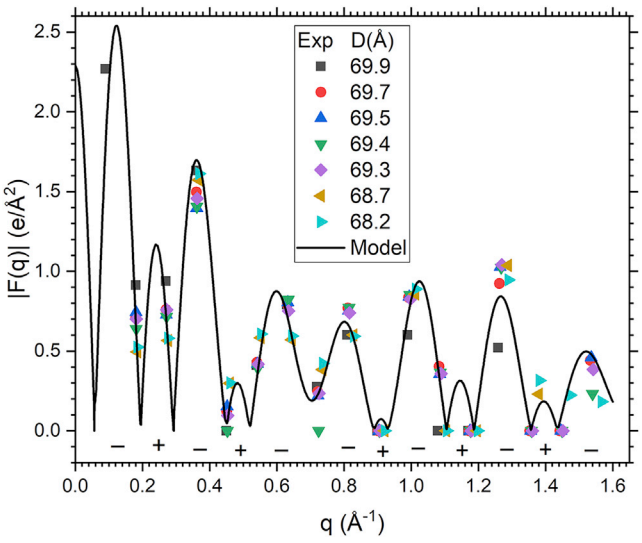

FIGURE 4 Experimental absolute values of scaled form factors F(q) for seven exposures with D-spacings as shown in the legend. The electron density model fit, shown as a continuous curve, is for the parameters in column 2 of Table 2. To see this figure in color, go online.

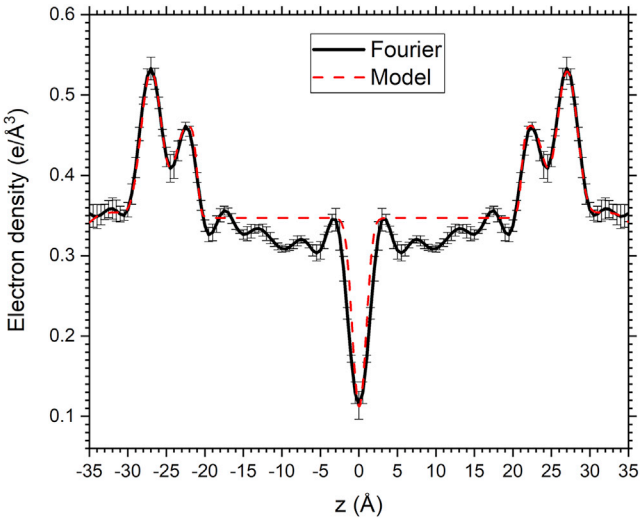

FIGURE 5 Electron densities $\rho(z)$. The black Fourier curve is the average of seven data sets with standard (correlated) deviations. The dashed red curve is from a model that has comparable deviations (not shown). To see this figure in color, go online.

methylenes, which is consistent with the wide-angle model in Fig. 1.

The Fourier construction does not by itself give absolute values of $\rho(z)$ using Eq. (2) for two reasons. The most important is the unknown scaling factor K_e in Eq. (3). This is determined by fitting a model using Eq. (5). The model that was chosen for Figs. 4 and 5 is shown in Fig. 6. It has three headgroup components, a phosphate, a choline, and a combined carbonyl glycerol. The value of V_L used in the model is shown in column 2 of Table 2. The agreement in the headgroup region is very good and that, along with the methyl trough, has the strongest influence on the F(q) in Fig. 4. The highest peak in the electron density profile is due to the phosphate group, and the second highest peak is associated with the carbonyl glycerol. The two headgroup peaks overlap less than in typical gel phases (25,38) and much less than in fluid phases (20,29), which again indicates that this gel phase is highly ordered. The sharp CG/methylene boundary is consistent with the WAXS model in Fig. 1. The model assumes that the methylene/methine region has constant electron density. Consistent with the WAXS model, the difference between the methine and methylene electron densities is negligible, so no separate methine component was added. Also consistent with the WAXS model, the terminal methyl was partitioned into a methylene that was then added to the other methylenes. The leftover electron was treated as a separate component, like what was recently done for gel phase DPPC (26). The largest discrepancy between the model and the Fourier construction is that the model imposes a constant electron density in the methylene region. In contrast, the WAXS model and the LAXS Fourier construction have a larger ED in the methylene region closer to the headgroups.

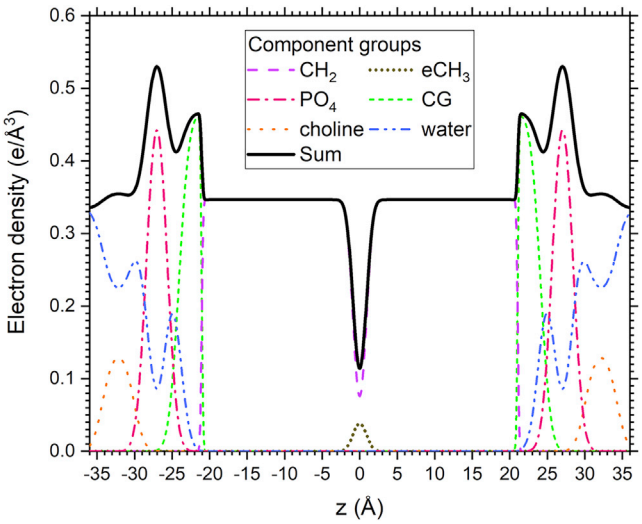

FIGURE 6 Contributions of the lipid components to the model electron density profile. CG abbreviates the carbonyls and glycerol. The terminal methyls are partitioned into a methylene and one excess electron designated as eCH_3. To see this figure in color, go online.

TABLE 2 LAXS results with units in the appropriate powers of Å. Column 3 gives values for gel phase DPPC at $T = 20^\circ$C for comparison (26). The parameters are defined in the text. The value of *D* is the average of those shown in Fig. 4 and *A* is from Table 1.

1	2	3
LAXS	diC22:1PC	DPPC
D	69.2 avg	63.2
A (WAXS)	47.6 (0.9)	47.3
$D_{HH}/2$	26.9 (0.2)	22.6
D_C	21.1 (0.2)	17.2
D_{H1}	5.6 (0.4)	5.1
V_{HC}	1003 (30)	814
V_H	331 fixed	331
V_L	1334 (30)	1144
D_B	56.1 (0.1)	48.4
n_W	10.4 (0.1)	11.7
V_{CH2}	22.8 (0.6)	25.9

Table 2 shows the average measured lamellar repeat spacing D, which is the best-determined quantity from LAXS data. The area per lipid A was obtained from the WAXS data. Other values for diC22:1PC in Table 2 are derived from the electron density model fit shown in Fig. 6. The spacing D_{HH} between the maxima in the electron density profile is quite robust when different models are chosen. The half-thickness D_C of the hydrocarbon region has uncertainties estimated by using different models of order 0.2 Å. The quantity D_{H1} is calculated as the difference $D_{HH/2} - D_C$. The volume of the hydrocarbon region $V_{HC} = AD_C$. The headgroup volume V_H was assumed to be the same as for DPPC. Summing V_{HC} and V_H gives the total lipid volume, V_L. The Luzzati thickness, D_B, and the number of water molecules per lipid, n_W, are derived as previously stated for Table 1.

DISCUSSION

The question that initially motivated this research was which features of lipid molecules give rise to ripple phases in bilayers. One hypothesis is that the headgroup size suffices to predict a ripple phase. This has been motivated by comparing lipids with the same saturated chains and different headgroups; phosphocholines (PCs) have a ripple phase, whereas the phospho-ethanolamines (PEs) that have a smaller headgroup, do not. Although a larger headgroup may be necessary for a ripple phase, our result that there is no ripple phase in diC22:1PC lipid bilayers shows that a large headgroup is not sufficient. A related property is that the larger PC headgroup forces saturated chains to tilt relative to the bilayer normal in the gel phase in contrast to the PEs (39). However, our result that diC22:1PC lipid tilts in the gel phase shows that tilt in the gel phase is also not a sufficient condition for a lipid bilayer to have a ripple phase.

Although we focus on the gel phase, which has a main chain melting transition at $T_M = 13°C$ into the fluid phase, we briefly report a new subgel phase in supporting material that appears to be the stable phase up to $T = 15°C$. However, it takes a long time to form, and our sample had some contaminating gel phase, so we have not pursued the structure of the subgel phase. Further, determining a subgel structure is a daunting task; even the structure of the much more studied subgel phase of saturated DPPC is incompletely determined (23). Although the gel phase of diC22:1PC is ultimately metastable, it is readily formed and does not decay into the subgel phase even for week-long experimental times. It is noteworthy that the metastability of the gel phase, characterized in Fig. S3, is similar to what occurs in DMPE (40).

Compared even to the best previously acquired data for any gel phase, the x-ray diffraction data for the diC22:1PC lipid gel phase are so striking that we could not resist performing a structural analysis. In particular, we know of no fully hydrated lipid bilayer for which 17 orders of diffraction have been reported, and the higher orders are quite strong. Qualitatively, having so many strong orders means that the diC22:1PC gel phase is highly ordered. If it were not for the cutoff of high-angle diffraction in our sample chamber, even more orders likely could have been measured.

The WAXS data provide the unit cell dimensions that directly provide two possibilities for the important lateral dimensions. Each gives the area per molecule A shown in Table 1. Obtaining a more detailed structure involves modeling. Not observing Bragg rods at distances compatible with lateral headgroup spacing and the lack of obvious in-plane correlation between neighboring bilayers strongly suggest that the observed Bragg rod scattering is due to chain packing. The presence of only two Bragg rods indicates that the in-plane unit cell is body-centered orthorhombic. Given the high degree of order suggested by the many strong LAXS orders, we have assumed that the chains are in their conformational ground state. From that assumption, efficient packing dictates that the z-positions of equivalent carbons be the same distance from the bilayer center. These include the double bonds of both chains in the unit cell and, therefore, both the *sn*-1 and *sn*-2 chains. This is quite different from the packing of straight all-*trans* saturated chains in gel phase DPPC, for which mini-interdigitation of the terminal methyl ends occurs (26), thereby allowing the *sn*-1 chain to penetrate more deeply than the *sn*-2 chain. This relative displacement of the two chains likely costs little packing energy in DPPC and that likely allows lower-energy headgroup conformations. However, a similar displacement of neighboring ground state C22:1 chains would necessarily incur such a large energy penalty that higher headgroup conformational energy could still be consistent with minimizing the total free energy.

Even after the assumptions in the preceding paragraph, there are still two ways for the two Bragg rods to be identified with the two in-plane dimensions, and for each of those, there are eight ways to symmetrize the monolayers to form a bilayer. None of those eight ways comes close to matching the intensity along the Bragg rods in Fig. 3 for unit cell UC1 in Table 1. The UC2 combination we have found to compare best to the WAXS data (Fig. 3) starts with mirror symmetry that is then broken by θ and ψ rotations of the chains and with offsets between the two monolayers, as shown in Fig. 1.

The many LAXS orders provide the opportunity to obtain accurate electron density profiles (EDP) in the transverse out-of-plane direction normal to the bilayer. The strategy we used for providing the electron density profile has previously been employed for the ripple phase of DMPC (41). Plausible electron density real-space models were Fourier transformed, and the real-space parameters were fit to obtain the best agreement with the measured intensities of the orders. The result shown in Fig. 4 determines the phase factors that we then used in a Fourier construction that only uses the experimental intensities as shown in Fig. 5, as well as the scaling factor provided by the model. This procedure reduces dependence on the functional form of the model. However, the fitted model shown in Fig. 6 also estimates where each lipid component resides in the bilayer.

The EDP provides an accurate and reliable value for an important measure of the bilayer thickness, D_{HH}, which is essentially the distance between the phosphates in the opposing monolayers. Another distance is the thickness $2D_C$ of the hydrocarbon core. The Fourier construction of the EDP in Fig. 5 suggests D_C in the range of 21 ± 0.5 Å, and the model fit shown in Table 2 gives $D_C = 21.1 \pm 0.5$ Å. These values agree well with the $D_C = 20.5 \pm 1.0$ Å value obtained from the entirely different model fit to the WAXS data in column 3 of Table 1.

An important datum that has been used in previous structure determination from this lab is the lipid volume V_L. Our

volume measurements are shown in Fig. S6 of the supporting material, but the poorly determined gel phase V_L is too large to be consistent with either kind of scattering data, WAXS or LAXS. For example, using the roughly measured volume $V_L = 1478$ Å^3 with our WAXS analysis results in a headgroup volume, $V_H = 502$ Å^3, that is larger than has ever been considered. And it infers a value of $F(0)$ via Eq. (4) that disagrees with the value of $F(0)$ shown in Fig. 4. However, the volume data were obtained for unoriented multilamellar vesicles (MLVs), whereas our high-quality x-ray data were obtained from stacks of bilayers. We have obtained x-ray data on MLVs that also has a different and more disordered pattern of peak intensities. Therefore, we conclude that the gel phase of C22:1PC has a different structure in MLVs than in oriented stacks.

We suggest that the reason for this discrepancy is that the intrinsic curvature in MLVs makes it difficult to obtain the highly ordered structure seen in stacks. An MLV basically consists of concentric spheres, and the innermost sphere has considerable curvature. In contrast, the structure of bilayers in a stack is not affected by curvature. Although the first bilayer in the stack is likely strongly affected by the substrate, chain packing in the subsequent 1600 bilayers is likely not to be affected. Since the significance of this study is to provide tests for simulations and most simulations are on flat membranes, we believe that gel phase C22:1PC structural data from stacks is more relevant than data from MLVs.

Therefore, instead of using the measured V_L, which we can only obtain from MLVs (or ULVs that are also highly curved), we propose that the relevant stack structure is represented by the values in column 3 of Table 1 and column 2 of Table 2. The area A is directly determined from WAXS. The separate analyses of WAXS and LAXS data yield about the same hydrocarbon thickness D_C. The parsing of the total lipid volume V_L into V_{HC} and V_{HC} is different for WAXS and LAXS, but the value of V_L is about the same. We suggest that final estimates of uncertainties in these quantities are given by the differences in their values in Tables 1 and 2. The average methylene volume V_{CH2} shown in Table 2 is also of interest for this discussion because it is significantly smaller than for the DPPC gel phase. This difference can be seen in the comparison of the EDP of DPPC and diC22:1PC shown in Fig. S5. DPPC chains are usually considered to be at least partially disordered with respect to different angles of rotation φ about the chain plane long axis for neighboring chains (42). Such disorder would be expected to increase V_{CH2} of DPPC relative to a more crystalline packing of neighboring chains. In contrast neighboring chains diC22:1PC cannot have different φ without incurring very large packing energy, so they would have a smaller V_{CH2} of more crystalline packing. Indeed, the value of V_{CH2} in column 2 of Table 2 is within the range of 22–24 Å^3 for highly ordered phases given in Table 5 of Nagle et al. (43). Fig. S5 also emphasizes that C22:1PC gel phase bilayers are thicker than DPPC and that the two headgroup peaks are more differentiated.

The two monolayers are correlated in our chain packing structure shown in Fig. 1. We have also performed calculations on other symmetries between the two monolayers and did not find a superior one to compare to the data in Fig.3. We have also calculated WAXS intensities for uncorrelated monolayers with the result that the calculated peaks in BR1 became too wide in q_z and could not be split into two nearly equal peaks.

Our chain structure raises an interesting question about what interaction causes the correlated orientations of monolayers in gel phases. DPPC has mini-interdigitation at the midplane due to the different penetration of the *sn*-1 and *sn*-2 chains. That might provide complementary rough surfaces to bring about correlated orientation. However, our structure of diC22:1PC monolayers has rather smooth faces made up of methyl groups at the same distance from the midplane. Accordingly, the methyl trough in the electron density profile is narrower for diC22:1PC, as can be seen in Fig. S5. It appears that there must be some interaction other than mini-interdigitation that brings about correlated monolayers in diC22:1PC.

Future research could build a model that includes headgroups and that evaluates its energetics using established force fields. A challenge will be to find headgroup conformations that connect stereo-chemically to a highly ordered hydrocarbon chain structure. The headgroup conformations will likely have higher energies on average than the conformations in the fluid phase, but the lower energy of chain packing will compensate for that. Such a study may illustrate the effect of competing interactions arising from different parts of heterogeneous lipids in bringing about structures of different phases. We suggest that it may be difficult for an MD simulation starting from scratch to find such a highly ordered state. A possibly more successful alternative would be to start with our structural model and then allow it to relax energetically. If this leads to a structure whose form factors and wide-angle pattern agree with the experimental data in Fig. 2, then that would be a better and more complete structure, and it would provide further validation of the force field.

SUPPORTING MATERIAL

Supporting material can be found online at https://doi.org/10.1016/j.bpj.2022.12.030.

AUTHOR CONTRIBUTIONS

Data were acquired by J.N., W.Q., and S.T. N.J. and J.N. analyzed the WAXS data. W.Q., D.Y., F.H., and J.N. analyzed the LAXS data. J.N., S.T., and F.H. wrote the paper.

ACKNOWLEDGMENTS

J.F.N. and S.T.N. dedicate this paper to our sometime co-author and friend Klaus Gawrisch and hope that it lives up to the high standard of attention to

detail for which he is famous. We thank beamline scientist Richard Gillilan for making possible our remote collection of x-ray scattering data at the ID7A1 station of the Cornell High Energy Synchrotron Source (CHESS), which is supported by the National Science Foundation and the National Institutes of Health/National Institute of General Medical Sciences under National Science Foundation Award DMR-0225180. F.H. acknowledges contributions from Alyssa Thomas and David P. Hoogerheide in implementing the model used for the analysis of the LAXS data. F.H. acknowledges support from the US Department of Commerce (Award 70NANB17H299). Certain commercial materials, equipment, and instruments are identified in this work to describe the experimental procedure as completely as possible. In no case does such identification imply a recommendation or endorsement by NIST, nor does it imply that the materials, equipment, or instrument identified are necessarily the best available for the purpose.

DECLARATION OF INTERESTS

The authors declare no competing interests.

REFERENCES

1. Tardieu, A., V. Luzzati, and F. C. Reman. 1973. Structure and polymorphism of hydrocarbon chains of lipids - study of lecithin-water phases. *J. Mol. Biol.* 75:711–733.
2. Small, D. M. 1986. The Physical Chemistry of Lipids, from Alkanes to Phospholipids. Plenum Press.
3. Nagle, J. F., and S. Tristram-Nagle. 2000. Structure of lipid bilayers. *Biochim. Biophys. Acta.* 1469:159–195.
4. Klauda, J. B., R. M. Venable, R. W. Pastor…, 2010. Update of the CHARMM all-atom additive force field for lipids: validation on six lipid types. *J. Phys. Chem. B.* 114:7830–7843.
5. Chiu, S. W., S. A. Pandit, E. Jakobsson…, 2009. An improved united atom force field for simulation of mixed lipid bilayers. *J. Phys. Chem. B.* 113:2748–2763.
6. Jämbeck, J. P. M., and A. P. Lyubartsev. 2012. Derivation and systematic validation of a refined all-atom force field for phosphatidylcholine lipids. *J. Phys. Chem. B.* 116:3164–3179.
7. Dickson, C. J., R. C. Walker, and I. R. Gould. 2022. Lipid21: complex lipid membrane simulations with AMBER. *J. Chem. Theor. Comput.* 18:1726–1736.
8. Poger, D., and A. E. Mark. 2010. On the validation of molecular dynamics simulations of saturated and cis-monounsaturated phosphatidylcholine lipid bilayers: a comparison with experiment. *J. Chem. Theor. Comput.* 6:325–336.
9. Sachs, J. N., H. I. Petrache, and T. B. Woolf. 2003. Interpretation of small angle X-ray measurements guided by molecular dynamics simulations of lipid bilayers. *Chem. Phys. Lipids.* 126:211–223.
10. Zhuang, X., J. R. Makover, J. B. Klauda…, 2014. A systematic molecular dynamics simulation study of temperature dependent bilayer structural properties. *Biochim. Biophys. Acta.* 1838:2520–2529.
11. Ulmschneider, J. P., and M. B. Ulmschneider. 2009. United atom lipid parameters for combination with the optimized potentials for liquid simulations all-atom force field. *J. Chem. Theor. Comput.* 5:1803–1813.
12. Cherniavskyi, Y., S. Baoukina, P. Tieleman…, 2017. Software for direct comparison of membrane scattering experiments data to molecular dynamics simulations. *Biophys. J.* 112:81a.
13. Venable, R. M., B. R. Brooks, and R. W. Pastor. 2000. Molecular dynamics simulations of gel (L-beta I) phase lipid bilayers in constant pressure and constant surface area ensembles. *J. Chem. Phys.* 112:4822–4832.
14. Tjörnhammar, R., and O. Edholm. 2014. Reparameterized united atom model for molecular dynamics simulations of gel and fluid phosphatidylcholine bilayers. *J. Chem. Theor. Comput.* 10:5706–5715.
15. Khakbaz, P., and J. B. Klauda. 2018. Investigation of phase transitions of saturated phosphocholine lipid bilayers via molecular dynamics simulations. *Biochim. Biophys. Acta Biomembr.* 1860:1489–1501.
16. de Vries, A. H., S. Yefimov, S. J. Marrink…, 2005. Molecular structure of the lecithin ripple phase. *Proc. Natl. Acad. Sci. USA.* 102:5392–5396.
17. Marrink, S. J., J. Risselada, and A. E. Mark. 2005. Simulation of gel phase formation and melting in lipid bilayers using a coarse grained model. *Chem. Phys. Lipids.* 135:223–244.
18. Tobias, D. J., K. Tu, and M. L. Klein. 1997. Atomic-scale molecular dynamics simulations of lipid membranes. *Curr. Opin. Colloid Interface Sci.* 2:15–26.
19. Wiener, M. C., and S. H. White. 1991. Fluid bilayer structure determination by the combined use of x-ray and neutron diffraction. I. Fluid bilayer models and the limits of resolution. *Biophys. J.* 59:162–173.
20. Kucerka, N., S. Tristram-Nagle, and J. F. Nagle. 2005. Structure of fully hydrated fluid phase lipid bilayers with monounsaturated chains. *J. Membr. Biol.* 208:193–202.
21. Kucerka, N., J. F. Nagle, J. Katsaras…, 2008. Lipid bilayer structure determined by the simultaneous analysis of neutron and x-ray scattering data. *Biophys. J.* 95:2356–2367.
22. Ruocco, M. J., and G. Shipley. 1982. Characterization of the sub-transition of hydrated dipalmitoylphosphatidylcholine bilayers - kinetic, hydration and structural study. *Biochim. Biophys. Acta Biomembr.* 691:309–320.
23. Raghunathan, V. A., and J. Katsaras. 1995. Structure of the L(C') phase in a hydrated lipid multilamellar system. *Phys. Rev. Lett.* 74:4456–4459.
24. Blaurock, A. E., and T. J. McIntosh. 1986. Structure of the crystalline bilayer in the subgel phase of dipalmitoylphosphatidylglycerol. *Biochemistry.* 25:299–305.
25. Tristram-Nagle, S., Y. Liu, …, J. F. Nagle. 2002. Structure of gel phase DMPC determined by X-ray diffraction. *Biophys. J.* 83:3324–3335.
26. Nagle, J. F., P. Cognet, S. Tristram-Nagle…, 2019. Structure of gel phase DPPC determined by X-ray diffraction. *Chem. Phys. Lipids.* 218:168–177.
27. Tristram-Nagle, S., R. Zhang, …, J. F. Nagle. 1993. Measurement of chain tilt angle in fully hydrated bilayers of gel phase lecithins. *Biophys. J.* 64:1097–1109.
28. Tristram-Nagle, S. 2007. Preparation of Oriented, Fully Hydrated Lipid Samples for Structure Determination Using X-Ray Scattering. Humana Press, Totowa, NJ.
29. Kucerka, N., Y. Liu, …, J. F. Nagle. 2005. Structure of fully hydrated fluid phase DMPC and DLPC lipid bilayers using X-ray scattering from oriented multilamellar arrays and from unilamellar vesicles. *Biophys. J.* 88:2626–2637.
30. Sun, W., R. M. Suter, …, J. F. Nagle. 1994. Order and disorder in fully hydrated unoriented bilayers of gel phase dipalmitoylphosphatidylcholine. *Phys. Rev. E.* 49:4665–4676.
31. Kucerka, N., S. Tristram-Nagle, and J. F. Nagle. 2006. Closer look at structure of fully hydrated fluid phase DPPC bilayers. *Biophys. J.* 90:L83–L85.
32. Nagle, J. F., K. Akabori, …, S. Tristram-Nagle. 2016. Determination of mosaicity in oriented stacks of lipid bilayers. *Soft Matter.* 12:1884–1891.
33. Smith, G. S., C. R. Safinya, N. A. Clark…, 1987. X-Ray study of freely suspended films of a multilamellar lipid system. *Mol. Cryst. Liq. Cryst.* 144:235–255.
34. Nagle, J. F., and M. C. Wiener. 1989. Relations for lipid bilayers - connection of electron-density profiles to other structural quantities. *Biophys. J.* 55:309–313.

35. Shekhar, P., H. Nanda, …, F. Heinrich. 2011. Continuous distribution model for the investigation of complex molecular architectures near interfaces with scattering techniques. *J. Appl. Phys.* 110:102216–10221612.

36. Kirby, B. J., P. A. Kienzle, C. F. Majkrzak…, 2012. Phase-sensitive specular neutron reflectometry for imaging the nanometer scale composition depth profile of thin-film materials. *Curr. Opin. Colloid Interface Sci.* 17:44–53.

37. Zhang, R., R. M. Suter, and J. F. Nagle. 1994. Theory of the structure factor of lipid bilayers. *Phys. Rev. E.* 50:5047–5060.

38. Wiener, M. C., R. M. Suter, and J. F. Nagle. 1988. Structure of fully hydrated lipid bilayers. *Biophys. J.* 53:A129.

39. McIntosh, T. J. 1980. Differences in hydrocarbond chain tilt between hydrated phosphatidylethanolamine and phosphatidylcholine bilayers. *Biophys. J.* 29:237–245.

40. Wilkinson, D. A., and J. F. Nagle. 1984. Metastability in the phase-behavior of "dimyristoylphosphatidylethanolamine bilayers. *Biochemistry.* 23:1538–1541.

41. Akabori, K., and J. F. Nagle. 2015. Structure of the DMPC lipid bilayer ripple phase. *Soft Matter.* 11:918–926.

42. Nagle, J. F. 1993. Evidence for partial rotational order in gel phase Dppc. *Biophys. J.* 64:1110–1112.

43. Nagle, J. F., R. M. Venable, R. W. Pastor…, 2019. Revisiting volumes of lipid components in bilayers. *J. Phys. Chem. B.* 123:2697–2709.

Biophysical Journal, Volume *122*

Supplemental information

Structure of the gel phase of diC22:1PC lipid bilayers determined by x-ray diffraction

John F. Nagle, Nathaniel Jennings, Weiheng Qin, Daniel Yan, Stephanie Tristram-Nagle, and Frank Heinrich

Supplemental Information for

Structure of the Gel Phase of diC22:1PC Lipid Bilayers Determined by X-ray Diffraction

John F. Nagle,[1] Nathaniel Jennings,[1] Weiheng Qin,[1] Daniel Yan,[1] Stephanie Tristram-Nagle,[1] and Frank Heinrich[1,2]

[1]Department of Physics, Carnegie Mellon University, Pittsburgh, PA USA 15213
[2]Center for Neutron Research, National Institute of Standards and Technology, Gaithersburg, MD USA 20899

I. Phase behavior and the subgel phase

A sample incubated at 5 °C was rapidly transferred on a cold pack to the X-ray sample chamber held at 5 °C. The left side of Fig. S1 shows lamellar orders up to h=14 that indexed well to a lamellar repeat spacing D = 72.6 Å in the z direction perpendicular to the bilayers. More dramatic was the wide angle pattern that comes from order in the in-plane r directions as shown on the right side of Fig. S1. While gel phases generally have strong scattering from the hydrocarbon chains that occurs in the range q_r ~ 1.3 to 1.6 Å^{-1}, only subgel phases have the weaker Bragg rods seen at smaller q_r in Fig. S1 (1), so we call this the S phase of diC22:1PC.

The temperature was subsequently increased in steps to 8 °C, 10 °C and 12 °C without a notable change in the x-ray pattern. However, at T=13 °C, a second set of peaks with orders h=1-5, corresponding to D = 68.6 Å, appeared in coexistence with the S peaks. We identify these peaks as belonging to the fluid F phase because these are the peaks that ultimately remained upon melting the sample. At T = 13 °C, the relative intensities of the lamellar h-orders of the F phase were considerably smaller than those of the S phase, although the ratios varied depending upon which part of the sample was exposed to x-rays as the sample was moved laterally in the beam. Also, the D spacing of the F peaks varied systematically as the relative humidity was varied. We then expected the complete transition to occur upon small additional increases in temperature above 13 °C. Instead, the relative intensities of the two phases remained the same as temperature was gradually increased. Only when the temperature was increased from T=15 °C to T=16 °C did the S

peaks all disappear, leaving only F peaks, which were all uniformly much more intense than they had been at 13 °C.

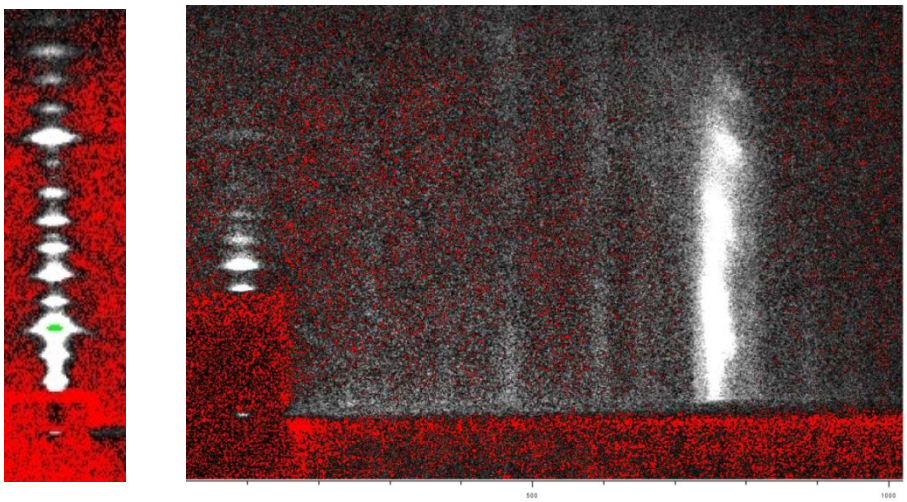

Fig. S1. Scattering from diC22:1PC bilayers in the S phase with background instrumentally subtracted. White pixels show high intensity. Red pixels indicate negative values after background subtraction. The left side shows lamellar orders h=2-14 in the q_z direction, taken while the sample was rotated in the beam; these give D = 72 Å. The right side was taken with the beam incident on the sample at the fixed angle of 0.5° with the very intense h=1-4 lamellar orders covered by the beam stop. In-plane scattering consists of Bragg rods at fixed q_r and variable q_z. The most intense WAXS scattering occurs on the Bragg rod at q_r = 1.42 Å^{-1}. Several additional weaker Bragg rods can also be discerned at q_r = 0.41, 0.65, 0.83, 1.1, 1.2, 1.45 and 1.7 Å^{-1}. Data were collected using a rotating anode.

The temperature was then lowered below T = 13 °C. The ensuing WAXS scattering pattern in Fig. 2 in the main text is considerably different from that in Fig. S1, and the intensities of the lamellar orders are also quite different as quantified in Fig. S2. Figure 2 shows two Bragg rods but no intermediate Bragg rods, so we call that the gel phase. As is also shown in Fig. S2, both ordered phases have stronger higher orders than the F phase; that is well understood as due to the smaller bending modulus of the F phase dispersing the intensity of the lamellar orders into diffuse scattering (2). Even after 3 days at T = 11 ° C, the S phase did not reappear. This is consistent with the nucleation and growth model that has been shown to apply to the DPPC subgel phase (3,4). To nucleate S domains within the experimenters' patience window, it is necessary to cool by an amount ΔT_S substantially below T_S. In the case of DPPC, ΔT_S is about six degrees (3). In the case of DiC22:1PC, we can only say that ΔT_S is between 3 °C and 8 °C because the subgel phase did not form at T = 10 °C, and 8 ° C because it did form at 5 °C, although only

after a long time. We conclude that a small portion of our original sample was in this ordinary low-temperature gel (G) phase that we subsequently showed does melt at the reported main transition at T_M = 13 °C and that most of the sample was originally in a subgel S phase that melted only at a temperature T_S higher than 15 °C. This implies that the S phase is the stable one below T_S and that the G phase is metastable at all temperatures. Fig. S3 shows qualitative free energy curves for this behavior.

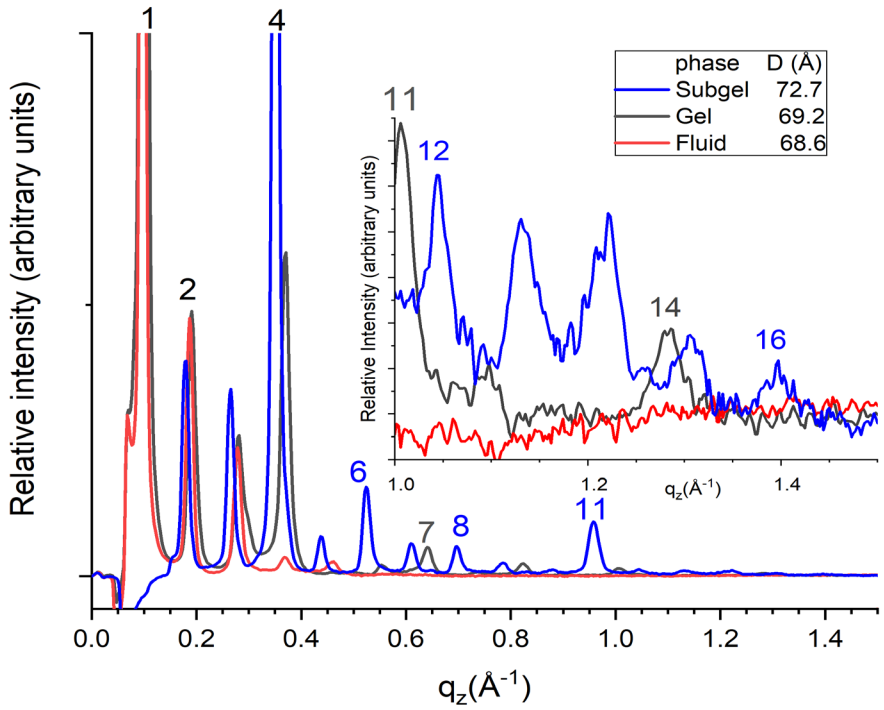

Fig. S2. Comparison of relative intensities of three phases, subgel, gel and fluid, with *D* spacings indicated in the legend. Some peak orders are marked by numbers *h*, denoting the order for the phases with higher order numbers color coded as indicated in the legend. The fluid phase intensities in red rapidly become much weaker as order h increases. The intensities of the gel and subgel are quite strong to much higher order, even before the Lorentz correction facto proportional to h.

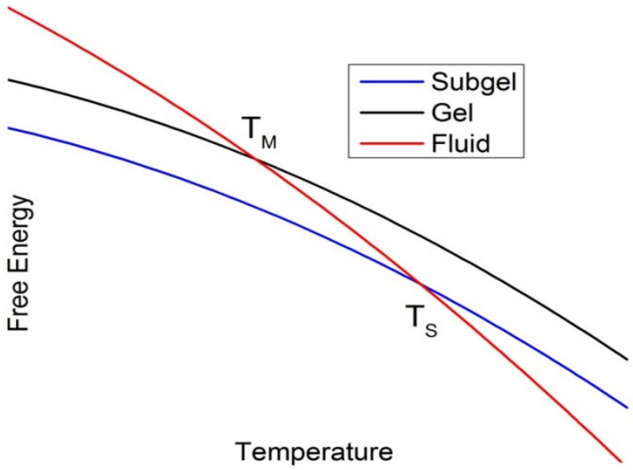

Fig. S3. Qualitative free energies of the three phases in this paper. The initial subgel phase melted into the fluid phase at $T_S \approx 16$ ºC. Upon cooling, the fluid phase transformed into the gel phase at $T_M = 13$ ºC. This thermal behavior is consistent with the sketch in which the gel phase is metastable to the subgel phase below T_M. A similar interpretation was proposed for the phase behavior of a different lipid (5).

II. Determination of intensities of weak peaks near strong peaks

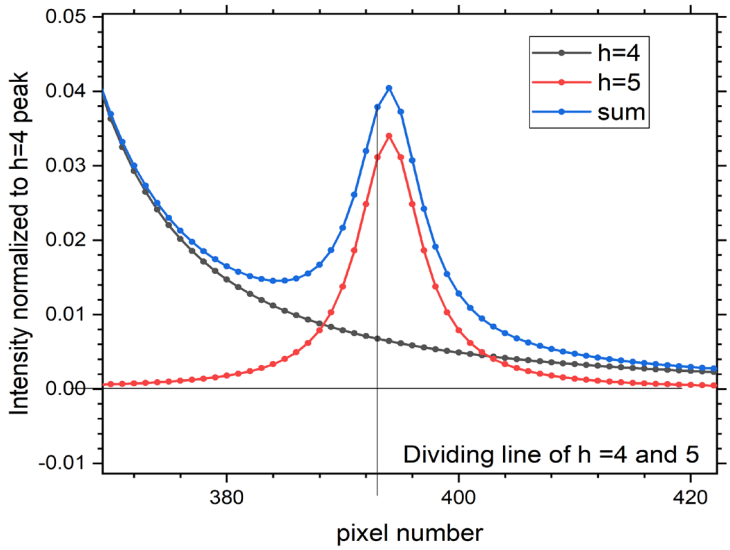

Fig. S4. The black curve is the tail of a Lorentzian with peak intensity 1.0 at pixel 353. The red curve is a Lorentzian for a weaker (h=5) peak. The true intensity of the weak peak is obtained by integrating the total intensity (blue) from the black line to higher pixel number. Integrating from the midpoint (at pixel 373) between the two peaks would more than double the h=5 intensity. Even integrating from the minimum of the blue curve would be a considerable overestimate.

III. Comparison of electron density profiles of DPPC and C22:1PC gel phases.

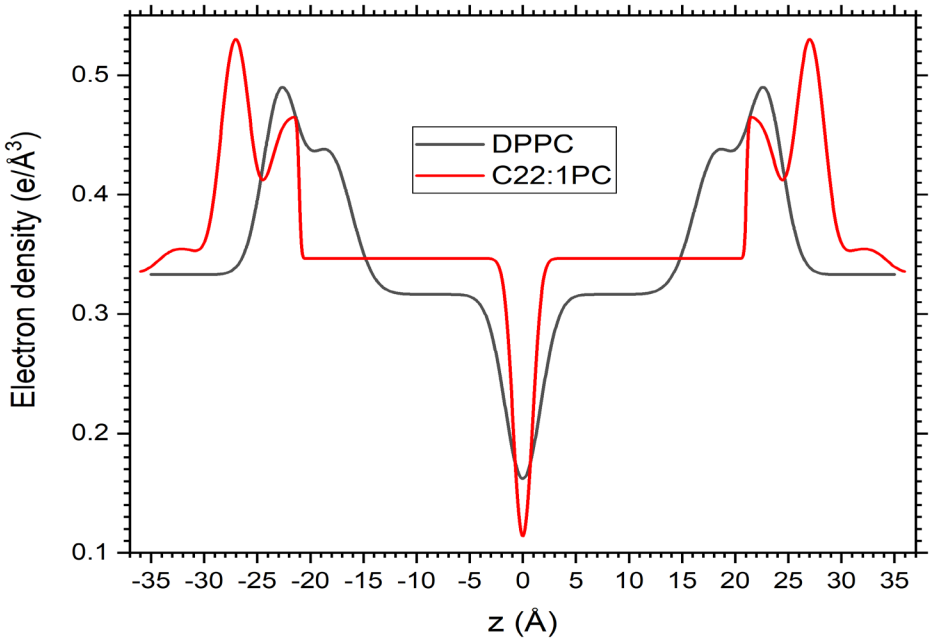

Fig. S5. Electron density versus distance along the normal to the bilayer. The red C22:1 curve is reproduced from the sum curve in Fig. 7, which uses the model in this paper, and the black DPPC curve is reproduced from Fig. 4 in (6), which used the SDP model (7). As expected for longer chains, the headgroups are further apart for C22:1PC, and the hydrocarbon plateau is longer. Because the chains are more tightly packed, the plateau is higher for C22:1PC. In addition, the smaller headgroup peak associated with the carbonyl-glycerol moiety is more differentiated from the highest peak, which is associated with the phosphate group. Finally, the width of the terminal methyl trough in the center of the bilayer is narrower for C22:1PC, consistent with all the methyls in each bilayer occurring the same distance from the center, whereas DPPC has mini-interdigitation (6).

IV. Molecular Volume

The volume of a lipid molecule V_L was measured in fully hydrated multilamellar (MLV) vesicles using an Anton-Paar USA DMA5000M (Ashland, VA) vibrating tube densimeter with a 1:20 lipid:water mass ratio. Figure S6 shows heating and cooling scans that agree very well with each other above the phase transition. Furthermore, the molecular volume agrees very well with the molecular volume of DOPC (1303 Å^3 at T = 30 ºC) (8) by adding eight methylene volumes (27.7 Å^3/methylene). In contrast, there was considerable hysteresis below the transition. We were concerned about the documented artifact incurred by the apparatus for gel phase DPPC, so we reloaded the sample many

times. However, the lipid density is close to that of water, so there was little driving force for the artifact observed in the DPPC gel phase (9). We also investigated time dependence for gel phase formation. We tentatively used $V_L = 1478$ Å^3 at T = 10 ºC. However, that value leads to strong contradictions between the WAXS and LAXS results. We then performed diffraction on oriented MLVs and found that the LAXS intensities were inconsistent with those shown in Fig. 4 for oriented stacks. We have concluded that MLVs and oriented stacks have different structures due to curvature incompatibility discussed in the text. Since we have no method to measure V_L for oriented stacks, the analysis in the text estimates it from the measured chain volume and an estimate of the head group volume.

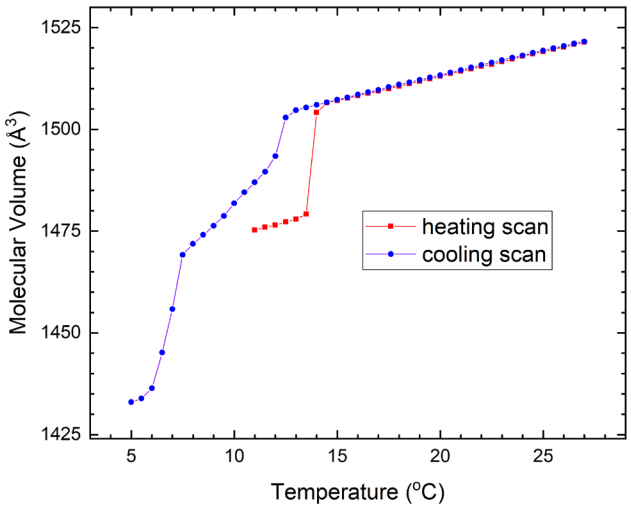

Fig. S6. Heating and cooling scans of molecular volume.

Bibliography

1. Raghunathan, V. A., and J. Katsaras. 1995. Structure of the L(C') Phase in a Hydrated Lipid Multilamellar System. *Phys Rev Lett*. 74(22):4456-4459, <Go to ISI>://A1995QZ97000025.
2. Zhang, R. T., R. M. Suter, and J. F. Nagle. 1994. Theory of the Structure Factor of Lipid Bilayers. *Phys Rev E*. 50(6):5047-5060, <Go to ISI>://A1994QA10800087.
3. Yang, C. P., and J. F. Nagle. 1988. Phase-Transformations in Lipids Follow Classical Kinetics with Small Fractional Dimensionalities. *Phys Rev A*. 37(10):3993-4000, <Go to ISI>://A1988N467000040.

4. Tristramnagle, S., R. M. Suter, W. J. Sun, and J. F. Nagle. 1994. Kinetics of Subgel Formation in Dppc - X-Ray-Diffraction Proves Nucleation-Growth Hypothesis. *Biochimica Et Biophysica Acta-Biomembranes*. 1191(1):14-20, <Go to ISI>://A1994NH54600003.
5. Wilkinson, D. A., and J. F. Nagle. 1984. Metastability in the Phase-Behavior of "Dimyristoylphosphatidylethanolamine Bilayers. *Biochemistry-Us*. 23(7):1538-1541, <Go to ISI>://A1984SK48400030.
6. Nagle, J. F., P. Cognet, F. G. Dupuy, and S. Tristram-Nagle. 2019. Structure of gel phase DPPC determined by X-ray diffraction. *Chem Phys Lipids*. 218:168-177, doi: 10.1016/j.chemphyslip.2018.12.011, <Go to ISI>://WOS:000459519000020.
7. Kucerka, N., J. F. Nagle, J. N. Sachs, S. E. Feller, J. Pencer, A. Jackson, and J. Katsaras. 2008. Lipid bilayer structure determined by the simultaneous analysis of neutron and x-ray scattering data. *Biophys J*. 95(5):2356-2367, doi: DOI 10.1529/biophysj.108.132662, <Go to ISI>://000258473900022.
8. Kucerka, N., S. Tristram-Nagle, and J. F. Nagle. 2005. Structure of fully hydrated fluid phase lipid bilayers with monounsaturated chains. *J Membrane Biol*. 208(3):193-202, doi: DOI 10.1007/s00232-005-7006-8, <Go to ISI>://000237193400001.
9. Hallinen, K. M., S. Tristram-Nagle, and J. F. Nagle. 2012. Volumetric stability of lipid bilayers. *Phys Chem Chem Phys*. 14(44):15452-15457, doi: 10.1039/c2cp42595e, <Go to ISI>://WOS:000310153300024.